Proceedings of the 21st ICSMGE, Vienna, Austria, 14 – 19 June 2026. Pistrol, Adam & Schweiger (eds.)
Published by: ÖGG, Austrian Society for Geomechanics, Salzburg, Austria, ISBN 978-3-9503898-4-5
https://doi.org/10.53243/ICSMGE2026-430

A computational approach for predicting large deformation of granular materials subjected to earthquake loading

Trieu N. Hoang & **Ha H. Bui**
Department of Civil and Environmental Engineering, Monash University, Melbourne, Australia, ha.bui@monash.edu

Giang D. Nguyen
School of Architecture and Civil Engineering, the University of Adelaide, Adelaide, Australia

Thang T. Nguyen & Tien V. Nguyen
Department of Civil and Environmental Engineering, Monash University, Melbourne, Australia

ABSTRACT: Earthquakes are natural disasters with the potential to cause significant damage to geotechnical structures. Accurately predicting the risks and potential damages from such events remains a considerable challenge, requiring advanced numerical tools capable of modelling the large deformations and failure mechanisms of geomaterials under seismic loading. In this study, we propose an advanced computational approach to effectively address this issue. Specifically, the general Smooth Particle Hydrodynamics (SPH) framework, incorporating an advanced bounding surface plasticity constitutive model, is employed to predict complex soil responses under cyclic loadings, including the evolution of excess pore water pressure within deformable porous media and the associated reduction in soil strength due to the loss of particle contacts. Appropriate non-reflecting boundary conditions are introduced for large deformation seismic response analyses of geotechnical problems. The SPH framework is first proven effective in simulating wave propagation and dissipation within geomaterials before being applied to investigate the failure process of field scale problems under seismic conditions. The simulation results provide valuable insights into the failure mechanisms, highlighting the advantage of the proposed SPH framework in quantitatively assessing seismic risks and their potential consequences. This research offers a robust tool for predicting and understanding the liquefaction phenomenon and associated large deformations under seismic conditions, thereby advancing geotechnical engineering and earthquake-induced disaster risk mitigation.

KEYWORDS: Smoothed Particle Hydrodynamics, earthquakes, large deformations, non-reflecting boundary, soil liquefaction.

1 INTRODUCTION

Seismic events often lead to severe deformation and failure of geomaterials, resulting in catastrophic impacts on geotechnical infrastructure and human life. Numerous past earthquakes have demonstrated the destructive potential of seismic loading on both natural and man-made systems (Seed et al., 1975; Inagaki et al., 1996). These consequences have prompted geotechnical engineers to place significant emphasis on seismic hazard assessment and the development of effective mitigation strategies. Central to this effort is the ability to simulate the highly nonlinear deformation behaviour in soils during earthquakes, which is vital for evaluating potential risks and estimating geotechnical structure damage. For this purpose, many numerical approaches have been developed over the years. Conventional mesh-based numerical methods, such as the finite element and finite difference methods, have been widely adopted for seismic response analysis in geotechnical engineering. However, these techniques are known to encounter difficulties when subjected to large deformation scenarios, particularly due to mesh distortion and entanglement. To overcome this limitation, mesh-free methods have gained significant attention, offering improved numerical stability and flexibility in capturing extreme deformation and complex failure mechanisms of geomaterials. Among these, the Smoothed Particle Hydrodynamics (SPH) method has emerged as a promising approach for modelling highly nonlinear and large deformation responses of geomaterials (Bui & Nguyen, 2021). Originally developed in the field of astrophysics, SPH has been successfully developed to solve a wide range of geotechnical engineering problems, including soil column collapse (Bui et al., 2008), slope failures (Bui & Nguyen, 2021), embankment failures (Bui & Fukagawa, 2013), soil structure interaction (Bui et al., 2014), rainfall-induced landslide (Nguyen et al., 2025), and erosion-induced soil failures (Ma et al., 2022). Despite its potential, the application of SPH in seismic response analysis remains relatively underexplored. One of the earliest attempts in this area was conducted by Bui et al. (2010), who applied seismic input motions directly to each SPH particle to simulate earthquake-induced slope failure. To improve the simulation of seismic wave propagation through soil media, later studies prescribed seismic loading at the model boundaries using the moving boundary approach (Chen & Qiu, 2014). However, these simulations typically relied on rigid boundary conditions, which caused undesirable wave reflections and reduced the accuracy of the simulated seismic responses. To overcome this limitation, Hoang et al. (2024) recently introduced SPH non-reflecting boundaries, significantly improving the accuracy of seismic wave propagation modelling. By incorporating the SANISAND model within the SPH framework, they demonstrated the capability of the approach in reproducing pre-liquefaction soil behaviours, including hysteretic response, excess pore-water pressure generation, and the reduction of mean effective stress. Nevertheless, the accumulated shear strain and associated degradation of strength and stiffness remained inadequately captured due to limitations of the SANISAND model in representing large post-liquefaction deformations. To address these gaps, this study presents our recent enhanced SPH framework for large deformation seismic response analysis of geotechnical systems. The proposed framework incorporates the advanced SANISAND-Sf constitutive model, capable of capturing cyclic mobility, strength degradation, and large post-liquefaction deformations. Appropriate free-field and compliant base SPH boundary conditions are implemented to effectively minimise artificial wave reflections, thereby ensuring more accurate simulations of seismic wave propagation. This development enables the robust simulation of field-scale, large deformation problems and contributes toward improving the seismic performance assessment of geotechnical systems.

2 NUMERICAL METHOD

2.1 *SPH approximation of governing equations*

In the SPH method, the computational domain is represented by a set of discrete particles that carry physical quantities such as mass, velocity, density, and stress of the material. These properties at a given material point are approximated by a kernel-based interpolation that makes use of information from neighbouring particles. The SPH method approximates a field function, its gradient, and the Laplacian operator in the following way (Bui & Nguyen, 2021),

$$f(\mathbf{x}_i) \approx \sum_{j=1}^{N} V_j f(\mathbf{x}_j) W(\mathbf{x}_i - \mathbf{x}_j, h_{sml}) \tag{1}$$

$$\nabla f(\mathbf{x}_i) \approx \sum_{j=1}^{N} V_j \left(f(\mathbf{x}_j) - f(\mathbf{x}_i) \right) \widetilde{\nabla}_i W_{ij} \tag{2}$$

$$\nabla^2 f(\mathbf{x}_i) \approx \frac{2}{K_{ij}} \left[\sum_{j=1}^{N} V_j f_{ji} \frac{\mathbf{x}_{ji} \cdot \nabla_i W_{ij}}{|\mathbf{x}_{ji}|^2} - \sum_{j=1}^{N} V_j f_{ji} \widetilde{\nabla}_i^{\alpha} W_{ij} \sum_{j=1}^{N} V_j \mathbf{x}_{ji}^{\alpha} F_{ij} \right] \tag{3}$$

where i denotes the target particle; j denotes the neighbouring particle; N denotes the number of neighbouring particles within the influence radius of the target particle; V is the volume occupied by a given particle; f_{ji} is the difference in field values; $\mathbf{x}_{ji}$ is the position vector from i to j; the superscript α denotes the coordinate, and repeated indices imply summation; $W(\mathbf{x}_i - \mathbf{x}_j, h_{sml})$ is the kernel function, and the cubic spline kernel function is employed in this study (Monaghan, 1985); h_{sml} is the smoothing length; $\nabla_i W_{ij}$ is the gradient of the kernel function; $\widetilde{\nabla}_i W_{ij} = L_i \nabla_i W_{ij}$ represents the corrected gradient of kernel function; $L_i = \left[\sum_{j=1}^{N} V_j \nabla_i W_{ij} \otimes (\mathbf{x}_j - \mathbf{x}_i) \right]^{-1}$ is the corrected matrix; $K_{ij} = \frac{1}{2} \left[\sum_{j=1}^{N} V_j \left(x_{ji}^2 + y_{ji}^2 \right) F_{ij} \right]$ and $F_{ij} = \frac{\mathbf{x}_{ji} \cdot \nabla_i W_{ij}}{|\mathbf{x}_{ji}|^2}$ is a normalisation factors.

This study employs the *u-p* formulation to capture the coupled behaviour between solid phase (s) and water phase (w) of geomaterials under fully saturated conditions. The derivation and assumptions underlying this formulation have been detailed in the work of Chan et al. (2022). By employing the basic SPH approximations, the governing equations for saturated porous media based on the *u-p* formulation are discretised in the SPH context as follows (Hoang, Nguyen, et al., 2024),

$$\begin{aligned} \frac{dp_{wi}}{dt} &= \frac{K_w}{n} \Bigg\{ - \sum_{j=1}^{N} V_j \mathbf{v}_{sji} \widetilde{\nabla}_i W_{ij} + \frac{1}{g} \sum_{j=1}^{N} V_j \bar{k}_{ji} \frac{d^s \mathbf{v}_{sji}}{dt} \widetilde{\nabla}_i W_{ij} \\ &+ \frac{1}{\gamma_w} \left[\frac{2}{K_{ij}} \sum_{j=1}^{N} V_j \bar{k}_{ji} p_{wji} F_{ij} - \frac{2}{K_{ij}} \sum_{j=1}^{N} V_j k_{wi} p_{wji} \widetilde{\nabla}_i^{\alpha} W_{ij} \sum_{j=1}^{N} V_j \mathbf{x}_{ji}^{\alpha} F_{ij} \right] \\ &+ \frac{2}{K_{ij}} \left[\sum_{j=1}^{N} V_j \bar{k}_{ji} z_{ji} F_{ij} - \sum_{j=1}^{N} V_j k_{wi} z_{ji} \widetilde{\nabla}_i^{\alpha} W_{ij} \sum_{j=1}^{N} V_j \mathbf{x}_{ji}^{\alpha} F_{ij} \right] \Bigg\} \end{aligned} \tag{4}$$

$$\frac{d\mathbf{v}_{si}}{dt} = \sum_{j=1}^{N} V_j \left(\frac{\boldsymbol{\sigma}_i \widetilde{\nabla}_i W_{ij} + \boldsymbol{\sigma}_j \widetilde{\nabla}_i W_{ij}}{\rho_{ti}} + \mathbf{C}_{ij} \right) + \mathbf{f} \tag{5}$$

$$\frac{d^s n_i}{dt} = \sum_{j=1}^{N} V_j (1 - n_j) (\mathbf{v}_{sj} - \mathbf{v}_{si}) \widetilde{\nabla}_i W_{ij} \tag{6}$$

where n represents the porosity of material; $\mathbf{v}$ denotes the velocity vector; ρ_t is the density of the mixture; $\boldsymbol{\sigma}$ denotes the total stress tensor, which is calculated as $\boldsymbol{\sigma} = \boldsymbol{\sigma}' - p_w \mathbf{I}$, with $\boldsymbol{\sigma}'$ is the effective stress tensor and p_w is the pore water pressure; $\mathbf{f}$ represents the external body force vector acting on the mixture; K_w denotes the bulk modulus of the water phase; γ_w is the specific weight of water; k_w denotes the coefficient of permeability; z denotes the elevation; the operator $\mathrm{d}/\mathrm{d}t$ refers to the material derivative; and the term $\mathbf{C}_{ij}$ includes numerical stabilisation terms like artificial viscosity and artificial stress, commonly adopted to avoid stress fluctuation and tensile instability in the SPH simulation (Bui et al., 2008). The Leap-Frog (LF) algorithm is employed to integrate the differential equations (Lian et al., 2023).

2.2 *SANISAND-Sf constitutive model*

In this study, the advanced SANISAND-Sf model is employed to simulate large post-liquefaction responses of granular materials (Barrero et al., 2020). A brief overview of key formulations underlying the model is outlined below. For a comprehensive derivation, readers are referred to the work of Barrero et al. (2020). The yield surface of the model is defined as a conical surface in principal stress space, characterised by the following function,

$$f = [(\mathbf{s} - p\boldsymbol{\alpha}) : (\mathbf{s} - p\boldsymbol{\alpha})]^{1/2} - \sqrt{2/3} pm = 0 \tag{7}$$

where $\mathbf{s}$ denotes the deviatoric stress tensor; p denotes the mean effective stress; m is a model parameter controlling the size of the yield surface; and $\boldsymbol{\alpha}$ is the deviatoric back stress ratio tensor. The bounding and dilatancy surfaces are formulated as stress ratio expressions,

$$\boldsymbol{\alpha}_{\theta}^{b} = \sqrt{2/3} \left[g(\theta, c_m) M \exp(-n^b \psi) - m \right] \mathbf{n} \tag{8}$$

$$\boldsymbol{\alpha}_{\theta}^{d} = \sqrt{2/3} \left[g(\theta, c_m) M \exp(n^d \psi) - m \right] \mathbf{n} \tag{9}$$

where $\boldsymbol{\alpha}_{\theta}^{b}$ and $\boldsymbol{\alpha}_{\theta}^{d}$ are the image stress ratio tensor on the bounding and dilatancy surfaces, respectively; $g(\theta, c_m)$ is a interpolation function; θ is the Lode angle; c_m is a model parameter; M is the critical stress ratio in triaxial compression; ψ is the state parameter; n^b and n^d are model constants; and $\mathbf{n} = (\mathbf{r} - \boldsymbol{\alpha}) / \|\mathbf{r} - \boldsymbol{\alpha}\|$ is the unit norm tensor-valued direction.

The plastic strain rate tensor is determined using a non-associated flow rule of the form,

$$\dot{\boldsymbol{\varepsilon}}_p = \langle L \rangle \mathbf{R} = \langle L \rangle \left[B\mathbf{n} - C \left(\mathbf{n}^2 - \frac{1}{3} \mathbf{I} \right) + \frac{1}{3} D \mathbf{I} \right] \tag{10}$$

where $\langle L \rangle$ is the plastic multiplier; $\mathbf{R}$ is the direction of plastic strain development; B and C are coefficients that incorporate the influence of the Lode angle (Dafalias & Manzari, 2004); D is the dilatancy coefficient, which is given as,

$$D = A_d (\boldsymbol{\alpha}_{\theta}^{d} - \boldsymbol{\alpha}) : \boldsymbol{n} \tag{11}$$

where the coefficient A_d is calculated using Eq. (15). The kinematic evolution of $\boldsymbol{\alpha}$ in Eq. (7) is given by,

$$d\boldsymbol{\alpha} = \langle L \rangle (2/3) h (\boldsymbol{\alpha}_{\theta}^{b} - \boldsymbol{\alpha}) \tag{12}$$

where h is the plastic hardening modulus defined by,

$$h = b_0/(\boldsymbol{\alpha} - \boldsymbol{\alpha_{in}}):\boldsymbol{n} \tag{13}$$

where $\boldsymbol{\alpha_{in}}$ denotes the back stress ratio tensor at the reversal loading point; the coefficient b_0 is defined as,

$$b_0 = G_0 h_0 (1 - c_h e)(p/p_{at})^{-1/2} \tag{14}$$

where G_0, h_0, c_h are model constants.

To simulate soil liquefaction and cyclic mobility, Dafalias and Manzari (2004) proposed a fabric-dilatancy component, which is expressed as follows,

$$A_d = A_0(1 + \langle \boldsymbol{z}:\boldsymbol{n}\rangle) \tag{15}$$

$$d\mathbf{z} = -c_z\langle -d\varepsilon_v^p\rangle(z_{max}\mathbf{n} + \mathbf{z}) \tag{16}$$

where A_0 is a model parameter related to dilation response; $\mathbf{z}$ is the fabric dilatancy tensor; c_z and z_{max} are model parameters of the fabric tensor; and $d\varepsilon_v^p$ is the plastic volumetric strain increment.

In the SANISAND-Sf model, the Semifluidised (Sf) component is introduced in the formulations of plastic hardening modulus and dilatancy coefficients by modifying the coefficients b_0 and D as follows (Barrero et al., 2020),

$$b_0 = G_0 h_0^* (1 - c_h e)(p/p_{at})^{-1/2} \tag{17}$$

$$D = A_0^*(1 + \langle \boldsymbol{z}:\boldsymbol{n}\rangle)\left(\boldsymbol{\alpha}_\theta^d - \boldsymbol{\alpha}\right):\boldsymbol{n} \tag{18}$$

where h_0^* and A_0^* are the two new coefficients that include the Sf component. The formulations for determining these coefficients are given by,

$$h_0^* = h_0[(1 - \langle 1 - p/p_{th}\rangle)^{xl} + f_l] \tag{19}$$

$$A_0^* = A_0[(1 - \langle 1 - p/p_{th}\rangle)^{xl} + f_l] \tag{20}$$

where x and f_l are model constants and the default value of f_l is 0.01. The evolution of variable l can be expressed as,

$$dl = \langle L\rangle[c_l\langle 1 - p/p_{th}\rangle(1 - l)^{n_l}] - c_r l|d\varepsilon_v| \tag{21}$$

where c_l, n_l, c_r are model constants; and the default value of n_l is 8.

To numerically integrate the constitutive model, a return mapping algorithm based on the cutting plane method with substepping is adopted, ensuring accuracy and stability under large strain triggered by soil liquefaction. Further implementation details within the SPH framework can be found in the work of Hoang, Nguyen, et al. (2024).

2.3 *SPH boundary conditions*

The application of the SPH method to solve geotechnical problems requires the use of appropriate boundary conditions (Bui & Nguyen, 2021). In the context of seismic response analyses, Hoang, Bui, et al. (2024) developed free-field and compliant base SPH boundary conditions to accurately simulate wave propagation within geomaterials by reducing artificial wave reflections at the boundary. Detailed formulations and implementation procedures can be found in Hoang, Bui, et al. (2024). The free-field SPH boundary conditions are applied to the lateral boundaries of the main model to simulate the dynamic response of an infinite soil domain and to prevent reflection of stress waves. To achieve this, two independent free-field soil columns are generated adjacent to the main model. These columns are computed separately and provide free-field responses that are then imposed on the side boundaries of the main model. The corresponding stress conditions applied to the boundary particles of the main model are defined as follows,

$$\sigma_b^{\alpha'\beta'} = \sigma_{b,s}^{\alpha'\beta'} + \sigma_{b,ff}^{\alpha'\beta'} \tag{22}$$

where α' and β' denote the coordinate in the local coordinate system; $\sigma_{b,s}^{\alpha'\beta'}$ is the static stress tensor before the seismic analysis; $\sigma_{b,ff}^{\alpha'\beta'}$ is the stress conditions of the free-field boundary, which can be calculated as,

$$\sigma_{b,ff}^{\alpha'\beta'} = \begin{bmatrix} \sigma_{b,fd}^{x'x'} - \rho C_p\left(v_b^{x'} - v_f^{x'}\right) \\ \sigma_{b,fd}^{y'y'} \\ \sigma_{b,fd}^{z'z'} \\ \sigma_{b,fd}^{x'y'} - \rho C_s\left(v_b^{y'} - v_f^{y'}\right) \end{bmatrix} \tag{23}$$

where $\sigma_{b,fd}^{\alpha'\beta'}$ is the differential stress in the free-field column arising from seismic excitation, computed as the difference between the dynamic stress $\sigma_{f,d}^{\alpha'\beta'}$ and the static component $\sigma_{f,s}^{\alpha'\beta'}$ within the free-field particles; $v_b^{\alpha'}$ and $v_f^{\alpha'}$ are the velocity vectors of soil particles located at the boundary of the main model and within the free-field soil column, respectively; ρ is the density of the soil material; C_p and C_s are the propagation speeds of compressional and shear waves, respectively.

The compliant base boundary conditions are applied along the bottom boundary of the model to simultaneously prescribe the seismic input motion and absorb outgoing waves. The input ground motion is introduced as a stress time history, while viscous dashpots are incorporated into the boundary formulation to dissipate reflected wave energy. The stress conditions imposed on the boundary particles at the base are given by,

$$\sigma_b^{\alpha'\beta'} = \sigma_{b,s}^{\alpha'\beta'} + \sigma_{b,c}^{\alpha'\beta'} \tag{24}$$

where $\sigma_{b,c}^{\alpha'\beta'}$ is the stress conditions of the compliant base boundary, which is calculated as,

$$\sigma_{b,c}^{\alpha'\beta'} = \begin{bmatrix} 2\rho C_p v_{in}^{x'} - \rho C_p v_b^{x'} \\ \sigma_r^{y'y'} - \sigma_{r,s}^{y'y'} \\ \sigma_r^{z'z'} - \sigma_{r,s}^{z'z'} \\ 2\rho C_s v_{in}^{y'} - \rho C_p v_b^{y'} \end{bmatrix} \tag{25}$$

where v_{in} represents the velocity input associated with the seismic ground motion; v_b represents the velocity of the boundary particles in the main model; σ_r indicates the stress state at the model boundary during earthquake shaking, while $\sigma_{r,s}$ refers to the initial stress condition at the model boundary prior to the onset of seismic excitation.

3 VERIFICATION AND VALIDATION

3.1 *Verification of seismic wave propagation*

This section presents a verification study to evaluate the capability of the proposed SPH framework in simulating seismic wave propagation through geomaterials. The numerical model consists of a homogeneous slope resting on a foundation layer, as illustrated in Figure 1. The slope has a height of 10 m, with a 2:1 inclination. Both the slope and foundation are assumed to behave elastically, and their material properties are summarised in Table 1. A seismic input motion from the 1989 Loma Prieta earthquake, obtained from the PEER ground motion database, is applied at the base of the model (Figure 2).

The SPH simulation uses 23,250 particles generated in a uniform grid with a spacing of 0.2 m. In SPH, seismic response analysis of geotechnical problems is conducted in two stages

(Hoang, Bui, et al., 2024). First, a static analysis is performed to establish the initial stress state using the stress initialisation approach proposed by Bui and Fukagawa (2013). In this stage, free-slip boundary conditions are applied along the lateral sides, while a non-slip condition is enforced at the base. In the second stage, dynamic analysis is conducted. Free-field SPH boundary conditions (as described in Section 2.3) are applied on both lateral sides to simulate the far-field response and absorb outgoing seismic waves. At the base, a compliant boundary condition (see Section 2.3) is employed to impose the seismic input motion while preventing wave reflections.

To verify the accuracy of the SPH results, the finite element (FEM) analysis is also performed in Plaxis 2D using the same geometry, material parameters, and boundary conditions. For comparison between the SPH results and finite element solutions, three measuring points (points A and B, as shown in Figure 1) within the slope are selected. Horizontal velocity time histories at these points, computed in SPH, are compared against those obtained from the FEM analysis (illustrated in Figure 3). The comparison reveals a strong agreement between the two methods across the entire seismic event, thereby confirming that the SPH framework can accurately simulate seismic wave propagation within geomaterials.

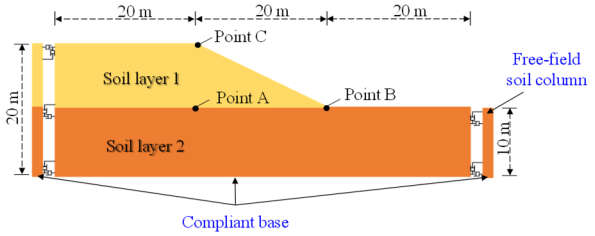

Figure 1. Slope geometry and dynamic boundary conditions.

Table 1. Parameters of soil layers within the slope.

Parameters	Soil layer 1	Soil layer 2
Elastic Modulus (E)	40 MPa	250 MPa
Poisson's ratio (ν)	0.35	0.25
Soil density (ρ)	1800 kg/m^3	2200 kg/m^3

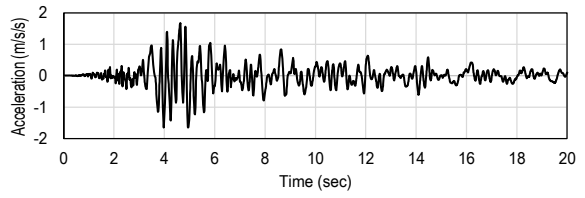

Figure 2. The input motion recorded from Loma Prieta earthquake.

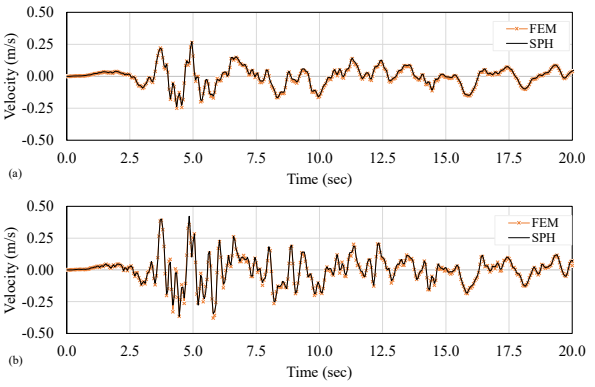

Figure 3. The seismic responses at measuring points: (a) Point A; (b) Point B.

3.2 *Validation of seismic ground response at the Sendai site*

The effectiveness of the proposed SPH-based approach in reproducing seismic wave propagation within the ground is further demonstrated through validation against a benchmark case from the PRENOLIN project (Régnier et al., 2018). The soil profile of the Sendai site is illustrated in Figure 4(a), while the corresponding SPH model is shown in Figure 4(b). The input motion corresponds to the downhole TS3 is used in the analysis (Régnier et al., 2018). In the SPH simulation, compliant base boundary conditions are applied at the bottom to both prescribe the seismic input motion and absorb outgoing waves, while the periodic boundary conditions are imposed on the lateral sides. The parameters used for the SANISAND-Sf model include the original SANISAND parameters adopted from the work of McAllister (2015) along with the additional parameters specific to the Sf component, as summarised in Table 2. Figure 5 presents a comparison between the SPH simulation results and recorded ground surface acceleration responses. The good agreement observed confirms the capability of the SPH-based approach to accurately capture the propagation of seismic waves through geomaterials.

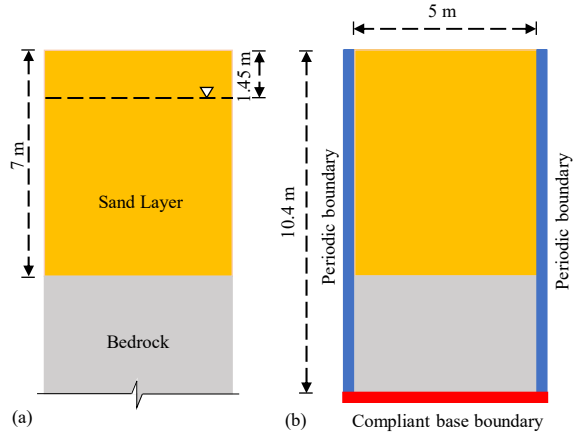

Figure 4. Sendai site benchmark case (a) Soil profile; (b) SPH model.

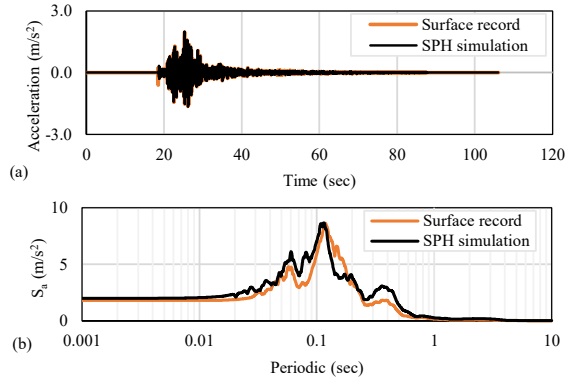

Figure 5. Comparisons of acceleration responses between SPH simulation results and field data.

4 SEISMICALLY LIQUEFACTION-INDUCED SLOPE FAILURE

The developed SPH framework, incorporating both free-field and compliant base SPH boundary conditions, has demonstrated its effectiveness in simulating seismic wave propagation within geomaterials. This section explores its further application in simulating earthquake-induced slope failure triggered by soil liquefaction.

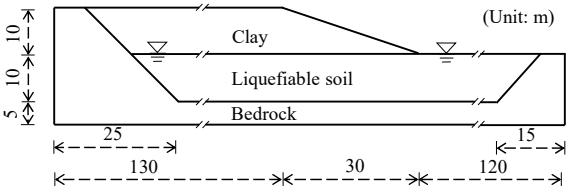

Figure 6. The slope model configuration.

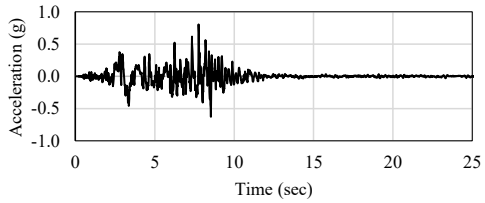

Figure 7. The input motion recorded from the San Fernando earthquake.

The slope model configuration is depicted in Figure 6 and consists of three different soil layers. The first layer is the clay slope, which has a thickness of 10 m and an inclination of 3:1. This layer rests on a 10 m thick liquefiable sand layer and beneath the sand is a rigid bedrock. This configuration of the slope is selected for demonstration purposes. In the SPH simulation, the computational domain is discretised using particles arranged initially in a regular square grid with a spacing of 0.5 m, resulting in a total of 23,550 particles representing the slope model. The slope is subjected to seismic motion recorded during the San Fernando earthquake in 1971. The input motion is presented in Figure 7 (PEER database), which is prescribed at the bottom boundary of the main model using the compliant base SPH boundary conditions as described in Section 2.3. On both sides of the main model, the free-field SPH boundary conditions, described in Section 2.3, are applied to force the free field motions and absorb the outgoing waves. To model the cyclic response and liquefaction behaviour of the sand layer, the SANISAND-Sf constitutive model is employed. Model parameters used in the simulation are listed in Table 2. The sand layer has an initial void ratio of 0.81, and an initial density of 2070 kg/m^3, a permeability of 0.01 cm/s, and a water bulk modulus of 1 GPa. The overlying clay layer is modelled using the Modified Cam Clay model, with corresponding parameters detailed in Table 3. The bedrock is assumed as a linear elastic material with the following soil properties: soil density of 2200 kg/m^3, elastic modulus of 250 MPa, and Poison's ratio of 0.25.

Table 2. SANISAND-Sf model constants.

Description	Symbol	Sendai sand	Liquefiable soil
Elasticity	G_0	125	125
	ν	0.05	0.05
Critical state	M	1.25	1.25
	c_m	0.672	0.712
	e_c^{ref}	0.9	0.934
	λ_c	0.279	0.019
	ξ	0.7	0.7
Yield surface	m	0.02	0.01
Dilatancy	n^d	3.5	3.5
	A_0	0.704	0.704
Kinematic	n^b	1.1	1.1
hardening	h_0	7.05	7.05
	c_h	0.968	0.968
Fabric	z_{max}	11	30
	c_z	1500	3000
Semifluidised	x	4	20
state	c_l	100	600
	p_{inr}	25 kPa	25 kPa

Table 3. Modified Cam Clay model constants for clay layer.

Soil layers	Parameters	Value
Clay	Swelling index (κ)	0.02
	Compression index (λ)	0.13
	Void ratio (e)	0.7
	Friction angle (ϕ)	25^o
	OCR	4
	Soil density (ρ)	2000 kg/m^3

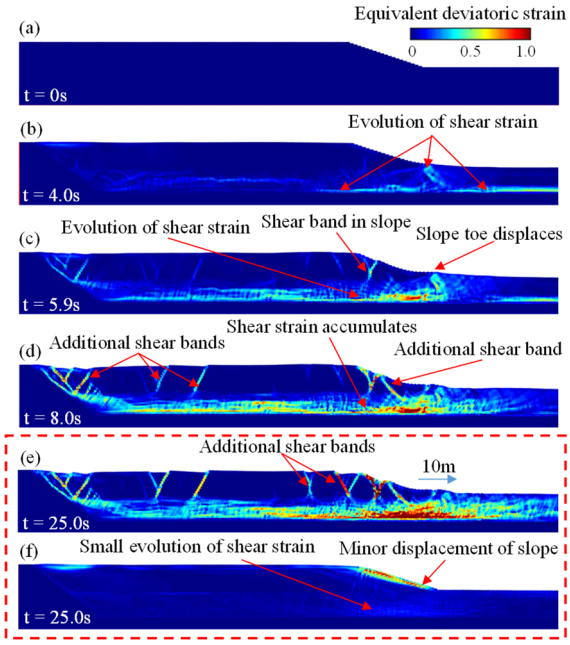

Figure 8. SPH simulation of the slope failure process: (a-e) results using SANISAND-Sf model; (f) result using original SANISAND model.

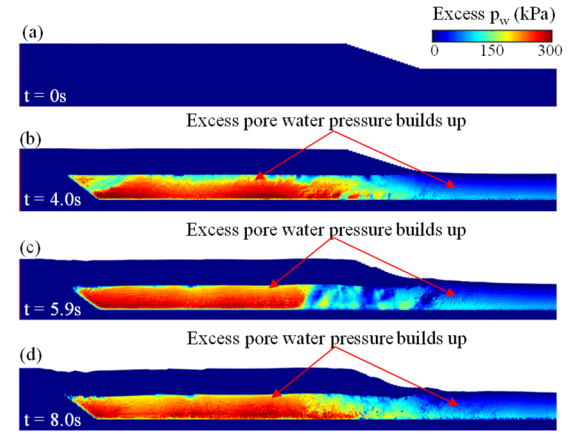

Figure 9. SPH simulation of excess pore water pressure evolution.

Figure 8(a-e) present the simulation results illustrating the progressive failure of the slope induced by the liquefaction of the underlying sandy soil layer during earthquake loading. Figure 9 illustrates the gradual build-up of excess pore water pressure within the liquefiable layer during cyclic loading. This indicates the corresponding decrease in mean effective stress towards the liquefaction state. During this pre-liquefaction stage, the slope remains stable until the sand layer enters the post-liquefaction stage at about $t \approx 4.0s$. Due to the reduction of soil strength and its stiffness in the Semifludised state, the plastic strain evolution is observed in the liquefiable layer. The large deformation of the liquefiable soil layer induces deformation in the overlaying clay, particularly near the slope toe (see Figure 8(c)). This deformation generates tensile forces

within the clay, triggering the formation of the initial shear bands, as illustrated in Figure 8(c). With continued shaking, plastic strain within the liquefiable soil layer accumulates with each loading cycle, driving further deformation in both the vertical and horizontal directions. As a result, the initial shear bands in the clay layer evolve and contribute to the progressive lateral displacement of the slope toe (see Figure 8(d)). With ongoing shaking, additional shear bands emerge within the clay, as shown in Figure 8(d). The final deformation profile of the slope is depicted in Figure 8(e), showing a lateral displacement of the slope toe approaching 10 m. The observed failure mechanism closely resembles lateral spreading failure commonly associated with earthquake-induced liquefaction (Youd, 1984). To highlight the enhanced capabilities of the proposed SPH framework with the advanced SANISAND-Sf model, its simulation results are compared with those from the original SANISAND model, as shown in Figure 8(f). It is observed that while the original model is capable of capturing liquefaction onset and associated deformation, it significantly underestimates the accumulation of shear strains during the post-liquefaction stage (see Figure 8(f)). This limitation arises from the model's inability to accurately reproduce the large post-liquefaction deformations observed in liquefiable soils (Barrero et al., 2020). In contrast, the SANISAND-Sf model enables more realistic simulation of shear strain accumulation and large post-liquefaction deformations.

5 CONCLUSIONS

This study presents an enhanced Smoothed Particle Hydrodynamics (SPH) framework for simulating large deformation seismic responses of geotechnical systems. Free-field and compliant base boundary conditions are incorporated to effectively eliminate artificial wave reflections, enabling accurate modelling of seismic wave propagation through saturated porous media. Furthermore, the advanced SANISAND-Sf constitutive model is incorporated for the first time in the SPH framework to capture key cyclic soil behaviours, including pore pressure generation, stiffness degradation, and large post-liquefaction deformations. The effectiveness and accuracy of the framework are verified through comparisons with small deformation finite element solutions and field data. Finally, the framework is applied to simulate the progressive failure of a slope triggered by soil liquefaction during a seismic event, successfully reproducing the large deformation mechanisms during both pre- and post-liquefaction. These findings highlight the substantial advancement of the present work over the earlier SPH framework incorporating the SANISAND model, confirming the robustness of the proposed approach as a predictive tool for assessing earthquake-induced geohazards.

6 ACKNOWLEDGEMENTS

The authors gratefully acknowledge support from the Australian Research Council via Discovery Projects, DP240102765 (Bui & Nguyen), FT200100884 (Bui), LP220200792 (Nguyen & Bui), and LP200100038 (Nguyen & Bui).

7 REFERENCES

Barrero, A. R., Taiebat, M., & Dafalias, Y. F. 2020: Modeling cyclic shearing of sands in the semifluidized state. *International Journal for Numerical and Analytical Methods in Geomechanics,* 44(3), 371-388.

Bui, H. H., & Fukagawa, R. 2013: An improved SPH method for saturated soils and its application to investigate the mechanisms of embankment failure: Case of hydrostatic pore-water pressure. *International Journal for Numerical and Analytical Methods in Geomechanics,* 37(1), 31-50.

Bui, H. H., Fukagawa, R., Sako, K., & Ohno, S. 2008: Lagrangian meshfree particles method (SPH) for large deformation and failure flows of geomaterial using elastic–plastic soil constitutive model. *International Journal for Numerical and Analytical Methods in Geomechanics,* 32(12), 1537-1570.

Bui, H. H., Fukagawa, R., Sako, K., & Okamura, Y. (2010). Earthquake induced slope failure simulation by SPH. The 5th Int. Conf. Rec. Advanced Geotech. Earthquake Eng., CD,

Bui, H. H., Kodikara, J. K., Bouazza, A., Haque, A., & Ranjith, P. G. 2014: A novel computational approach for large deformation and post-failure analyses of segmental retaining wall systems. *International Journal for Numerical and Analytical Methods in Geomechanics,* 38(13), 1321-1340.

Bui, H. H., & Nguyen, G. D. 2021: Smoothed particle hydrodynamics (SPH) and its applications in geomechanics: From solid fracture to granular behaviour and multiphase flows in porous media. *Computers and Geotechnics,* 138, 104315.

Chan, A. H., Pastor, M., Schrefler, B. A., Shiomi, T., & Zienkiewicz, O. C. (2022). *Computational geomechanics: theory and applications*. John Wiley & Sons.

Chen, W., & Qiu, T. 2014: Simulation of earthquake-induced slope deformation using SPH method. *International Journal for Numerical and Analytical Methods in Geomechanics,* 38(3), 297-330.

Dafalias, Y. F., & Manzari, M. T. 2004: Simple plasticity sand model accounting for fabric change effects. *Journal of Engineering mechanics,* 130(6), 622-634.

Hoang, T. N., Bui, H. H., Nguyen, T. T., Nguyen, T. V., & Nguyen, G. D. 2024: Development of free-field and compliant base SPH boundary conditions for large deformation seismic response analysis of geomechanics problems. *Computer Methods in Applied Mechanics and Engineering,* 432, 117370.

Hoang, T. N., Nguyen, T. T., Nguyen, T. V., Nguyen, G. D., & Bui, H. H. 2024: SPH simulation of earthquake-induced liquefaction and large deformation behaviour of granular materials using SANISAND constitutive model. *Computers and Geotechnics,* 174, 106617.

Inagaki, H., Iai, S., Sugano, T., Yamazaki, H., & Inatomi, T. 1996: Performance of caisson type quay walls at Kobe port. *Soils and Foundations,* 36, 119-136.

Lian, Y., Bui, H. H., Nguyen, G. D., & Haque, A. 2023: An effective and stabilised (u− pl) SPH framework for large deformation and failure analysis of saturated porous media. *Computer Methods in Applied Mechanics and Engineering,* 408, 115967.

Ma, G., Bui, H. H., Lian, Y., Tran, K. M., & Nguyen, G. D. 2022, 2022/11/01/: A five-phase approach, SPH framework and applications for predictions of seepage-induced internal erosion and failure in unsaturated/saturated porous media. *Computer Methods in Applied Mechanics and Engineering,* 401, 115614.

McAllister, G. (2015). *Nonlinear seismic ground response of shallow sand sites* University of British Columbia].

Monaghan, J. 1985: Extrapolating B splines for interpolation. *Journal of Computational Physics,* 60(2), 253-262.

Nguyen, D.-T., Bui, H. H., Lian, Y., Nguyen, T. T., Nguyen, G. D., & Bouazza, A. 2025: A CASM-X constitutive model for unsaturated soils and its application to model wetting-induced slope collapse using SPH. *Computers and Geotechnics,* 186, 107353.

Régnier, J., Bonilla, L. f., Bard, P. Y., Bertrand, E., Hollender, F., Kawase, H., Sicilia, D., Arduino, P., Amorosi, A., & Asimaki, D. 2018: PRENOLIN: International benchmark on 1D nonlinear site-response analysis—Validation phase exercise. *Bulletin of the Seismological Society of America,* 108(2), 876-900.

Seed, H. B., Idriss, I. M., Lee, K. L., & Makdisi, F. I. 1975: Dynamic analysis of the slide in the Lower San Fernando Dam during the earthquake of February 9, 1971. *Journal of the Geotechnical Engineering division,* 101(9), 889-911.

Youd, T. L. 1984: Geologic effects-liquefaction and associated ground failure. *Proceedings of the Geologic and Hydraulic Hazards Training Program*, 210-232.